Coupled polaron-phonon effects on Seebeck coefficient and lattice conductivity of B_{13}C_{2} from first principles

Hyoungchul Kim and Massoud Kaviany

Coupled Polaron-Phonon Effects on Seebeck Coefficient and Lattice Conductivity of B$_{13}$C$_2$ from First Principles

Hyoungchul Kim and Massoud Kaviany[*]

Department of Mechanical Engineering, The University of Michigan, Ann Arbor, MI 48109, USA
(Dated: April 1, 2013)

Anomalous temperature-independent behavior of the Seebeck coefficient and lattice thermal conductivity of B$_{13}$C$_2$ are explained through polaron and phonon evolutions found using *ab-initio* molecular dynamics (AIMD). Analyses of lattice dynamics show that the unique icosahedron structures dominate the optical phonon modes and CBC inter-icosahedral bonds dominate the local acoustic vibration. We identify that the temperature-induced Jahn-Teller distortion and electron-phonon coupling in icosahedron structures create the small polarons (i.e., charge trapping and phonon softening). We also verify that large-displacement chain atoms scatter heat-conducting phonons. Using equilibrium and non-equilibrium AIMD methods (including entropy and energy analyses), we predict the Seebeck coefficient and its components, and the lattice thermal conductivity, and find good agreement with experiments. Softened and localized phonons make significant vibrational contribution to the Seebeck coefficient and allow for an amorphous-like lattice thermal conductivity.

PACS numbers: 71.38.-k, 71.15.Mb, 72.20.-i, 73.50.Lw

I. INTRODUCTION

Widely used boron carbides (B$_{12+x}$C$_{3-x}$), e.g., in refractories, abrasives, thermoelectrics, nuclear reactors[1], have much unexplained structural and carrier transport properties. Their primitive cell ($R3m$ space group, rhombohedral representation) contains an icosahedron of twelve atoms with strong covalent chains connecting them, as shown in Fig. 1[1]. They are very similar to the pure α-B$_{12}$ structure, with an icosahedron and polar linkers, however the inter-icosahedral bonds are changed with the addition of carbon. So, boron carbides are hard solids with the melting temperature of $\sim$ 2600 K[1–3]. Due to their polymorphism, their crystal structure identification is still evolving[4], and they have high p-type carrier density ($\sim 10^{21}$ cm^{-3})[2,5]. Odd number of B atoms (e.g., $x = 1$) removes bound electrons, produces hole-like carriers (one hole per primitive cell) and the high hole density, while stoichiometric compounds B$_{12+x}$C$_{3-x}$ have moderate carrier density[3,6]. Their hardness and carrier density suggest large thermal conductivity ($\kappa = \kappa_e + \kappa_L$, dominated by lattice thermal conductivity κ_L), high electrical conductivity (σ_e), and small Seebeck coefficient (α_S), but they have small κ_L and large α_S, both nearly temperature independent[5,7–9]. Also, the small σ_e exponentially increases with temperature (T)[7,9].

To explain these anomalous properties, two models have been suggested by Emin *et al.*[2,5,10,11] and Werheit *et al.*[4,12]. The first is the small bipolaron model for the nonequivalent B$_{11}$C icosahedra, suggesting localized charge (q) carriers with low mobility, i.e., phonon-assisted polaron hopping. The second model is based on structural disorder in B$_{12}$-CBC, where the high density intrinsic defects accompanied by strong distortion compensate for the electron deficiency of ideal metallic behavior and also reduce κ. This structural conjecture is still evolving with the mentioned polymorphism[1,12], as reported in the phase diagram and diffraction results demonstrating the

abundances of phases[1]. The B$_{11}$C-CBC model is believed to be the lowest formation energy and the most relevant structure for $x = 0$, whereas the B$_{12}$-CBC is the most stable phase for $x = 1$[1,13,14]. Those structural models are verified from the formation energy calculation using the density-functional theory (DFT)[13–15]. Here we consider α-B$_{12}$ and B$_{13}$C$_2$ structures containing a B$_{12}$ icosahedron and a CBC inter-icosahedral chain, since they are the ground-state structures from the energetic (thermodynamic) perspective and because there is a distinct structural evolution with added carbon.
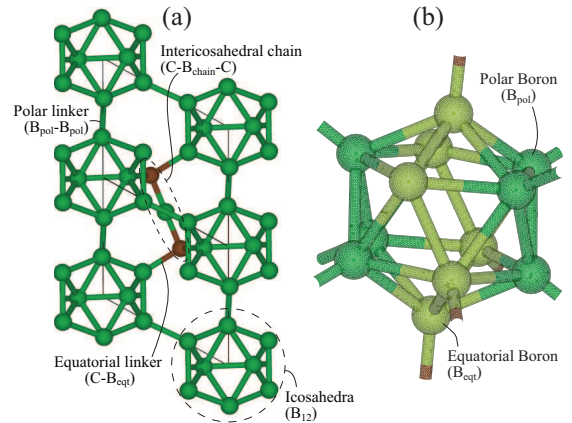

FIG. 1: (Color online) The crystalline structure of B$_{13}$C$_2$: (a) A primitive cell (B = green, C = brown) and (b) the magnified view of a B$_{12}$ icosahedron in B$_{13}$C$_2$ showing two different borons, the polar (B$_{pol}$; yellowish green) and the equatorial (B$_{eqt}$; dark green) atoms.

Here, we present a comprehensive theoretical/computational analyses of the polaron formation and phonon softening in B$_{13}$C$_2$, using *ab-initio* methods. We predict/explain the temperature independencies of α_S (including entropy analysis of various contributions) and κ_L, and compare with available experimental results.

Our results show such anomalous behaviors are caused by polaron and phonon evolutions due to the unique icosahedra and inter-icosahedral chains in $B_{13}C_2$.

II. CALCULATION METHODS

A. DFT calculations

We begin with the electronic structure and lattice dynamics using various DFT calculations implemented in the Vienna *ab-initio* simulation package (VASP)[16] and PHONON[17] codes. The Perdew-Burke-Ernzerhof parameterization of the generalized gradient approximation for the exchange-correlated functional[18] and the projector augmented wave method for modeling core electrons (energy cutoff = 520 eV)[19,20] are used. All phonon and thermodynamic properties are predicted using fits of interatomic force constant tensors to the calculated Hellmann-Feynman (HF) forces. The total energy and HF forces are found starting from the fully-relaxed configuration, such that initial ionic forces were less than 10^{-5} eV/Å. Ionic displacements of 0.03 Å of each atom were sampled along all three directions. Diagonalization of the dynamical matrix yields the phonon dispersion curves, density-of-states (D_p), and atomic displacement tensors. The atomic displacement parameter (ADP) is obtained from the trace of the diagonalized atomic displacement tensor.

The high-temperature lattice dynamics are investigated by equilibrium *ab-initio* molecular dynamics (EAIMD). The temperature-dependent phonon density-of-states are also obtained from EAIMD and the Fourier transform of the velocity autocorrelation function over 22 ps. EAIMD simulations are performed on supercells consisting of 180 atoms. Considering thermal expansion, we prepare supercells with the experimental thermal expansion coefficient (CTE = 5.73×10^{-6}/K for 300 to 1970 K)[21] and lattice parameter ($a = 5.63$ and $c = 12.16$ Å at $T = 300$ K)[1,21] are used. The Brillouin zone is sampled at the gamma point. After constant-temperature simulations with the Nosé thermostat for 1 ps (0.5 fs time step) reaching equilibrium, we collect atomic trajectories for 22 ps (1 fs time step).

To predict α_S and κ_L, we use non-equilibrium *ab-initio* molecular dynamics (NEAIMD). For non-equilibrium simulations, we use the VASP code modified to perform NEAIMD-energy exchange[22,23] as reported in[24,25]. The heat flux is imposed by dividing the simulation cell into sections of equal width, and exchanging kinetic energy (velocity swapping) between the hot and cold sections. Because the exchange of kinetic energy results in non-Newtonian dynamics in the hot and cold sections, only the linear portion of the temperature gradient is considered in calculating the temperature gradient. For further validation on the charge associated with each atom in the simulation cell (hot to cold), the Bader analysis[26] of charge-density grid is used with the DFT charge density. NEAIMD simulations are performed on (hexagonal representation) supercells consisting of 180, 270, and 360 atoms. Structure preparations are same with EAIMD simulations. We carry out constant-temperature simulations using a Nosé thermostat for 1 ps (0.5 fs time step). After reaching equilibrium, a non-equilibrium calculation is performed for 22 ps (1 fs time step).

The electron-phonon (*e-p*) coupling parameter is calculated from the self-consistent change in the potential of electrons interacting with a phonon mode implemented in the Quantum-ESPRESSO[27] package with norm-conserving pseudopotential and a plane-wave cut-off energy of 40 Ry. Fully-relaxed structures are simulated with an electron-momentum mesh of $8 \times 8 \times 8$ and a $4 \times 4 \times 4$ phonon-momentum mesh grid. The *e-p* coupling parameter is calculated from the self-consistent change in the potential of electrons interacting with a phonon mode[27]. Here the *e-p* interaction matrix $M_{k'_e,k_e}^{i,j,\nu}$ is

$$M_{k'_e,k_e}^{i,j,\nu} = \left(\frac{\hbar}{2m\omega_{k_e,k'_e}^{i,j}}\right)^{1/2} \langle \psi_{k'_e}^j \mid \delta\varphi_{k_p}^\nu \mid \psi_{k_e}^i \rangle, \quad (1)$$

where $\hbar$ is the reduced Planck constant, m is ion mass, ω is phonon frequency, $\delta\varphi_{k_p}^\nu$ is the phonon perturbation for a particular mode, and ψ is the wavefunction, k_e and k'_e are electron wave vectors with band indices i and j. k_p is phonon wave vectors with the mode number ν. The Eliashberg spectral function α^2F is defined as[14,28,29]

$$\alpha^2F = \frac{1}{D_e(E_F)} \sum_{k_e,k'_e,k_p} |M_{k'_e,k_e}^{i,j,\nu}|^2 \delta_D(E_{k_e}^i)\delta_D(E_{k'_e}^j)\delta_D(\omega-\omega_{k_p}^\nu), \quad (2)$$

where $D_e(E_F)$ is the density-of-states per atom and spin at the Fermi level, and δ_D is the delta function.

B. Entropy and energy analyses of Seebeck coefficient

The overall α_S can be expressed as sum of various contributions,

$$\alpha_S = \alpha_{S,mix} + \alpha_{S,spin} + \alpha_{S,vib} + \alpha_{S,trans}, \quad (3)$$

where the right hand side terms are: change of entropy-of-mixing, spin entropy, vibrational entropy upon adding a charge carrier, and the net energy transferred in moving a carrier (divided by qT), respectively[30]. Each carrier mostly contributes to α_S in different way and specific conditions, however they are highly coupled and interacting with phonon.

The mixing contribution to $\alpha_{S,mix}$ is usually related with electron and dominant in lightly-doped semiconductors. The $\alpha_{S,mix}$ is then related to the change of mixing entropy S_{mix} upon adding a carrier:

$$\alpha_{S,mix} = \frac{1}{q}\frac{\partial S_{mix}}{\partial N} = \frac{k_B}{q}\ln\left(\frac{1-f_e^\circ}{f_e^\circ}\right), \quad (4)$$
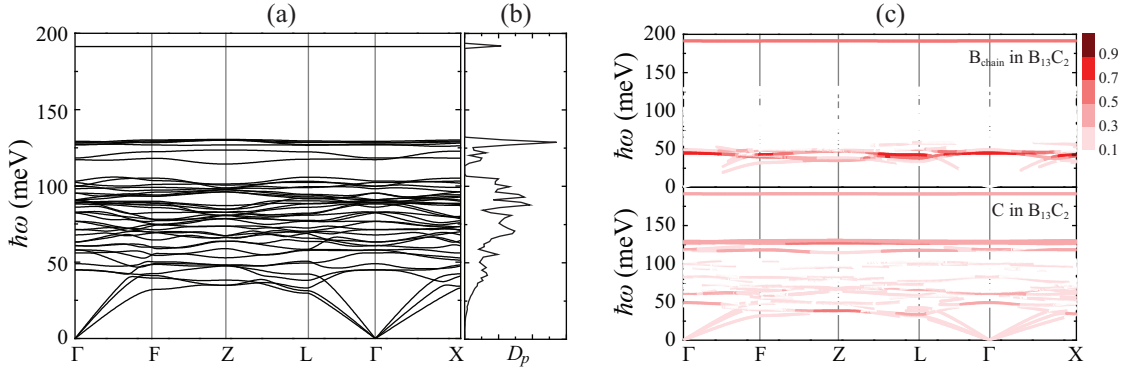
FIG. 2: (Color online) Calculated phonon characteristics of $B_{13}C_2$: Total phonon (a) dispersion curves and (b) density-of-states. (c) Projected phonon dispersion curves of B_{chain} (upper panel) and C (lower panel) atoms. Color key shows the scaled contribution (maximum of one) of each atom.

where k_B is the Boltzmann constant and $f_e^\circ = N/N_A$ is the ratio of electrons to sites (Fermi function)[6,30,31]. The spin entropy S_{spin} contribution to α_S is

$$\alpha_{S,spin} = \frac{\Delta S_{spin}}{q} = \frac{k_B}{q}\ln(\frac{2s+1}{2s_\circ+1}), \qquad (5)$$

where $s_\circ$ and s are net spins of the magnetic site in the absence and presence of the spin carrier[6,30].

For the $\alpha_{S,vib}$, reducing the local vibrational frequencies (phonon softening) increases the vibrational entropy (S_{vib}). The full crystal Hamiltonian (H) for the vibrational part of the energy is obtained by adding the potential and kinetic energy. We write the Hamiltonian (for the quantum-harmonic oscillator) as[31]

$$H_{vib} = \sum_{k_p} \hbar\omega(k_p)(f_p^\circ + \frac{1}{2}), \qquad (6)$$

where f_p° is the equilibrium occupancy of phonon. H_{vib} is used to solve analytically for thermodynamic properties, e.g., the free energy F_{vib} is $-k_B T \ln[\sum \exp(-H_{vib}/k_B T)]$, where the entropy is $S_{vib} = -\partial F_{vib}/\partial T$. The phonon density-of-states gives the number of modes with the frequency in the interval $[\omega, \omega + d\omega]$, and first-order contribution to the $\alpha_{S,vib}$ is[5,6,11,30]

$$\begin{aligned}\alpha_{S,vib} &= \frac{1}{q}\sum_i \frac{\partial S_{vib,i}}{\partial\omega_i}\Delta\omega_i \\ &= \frac{k_B}{q}\sum_i(\frac{-\Delta\omega_i}{\omega_i})[\frac{\hbar\omega_i/2k_B T}{\sinh(\hbar\omega_i/2k_B T)}]^2. \quad (7)\end{aligned}$$

From the high-temperature limit ($k_B T \gg \hbar\omega$) and series expansions of the hyperbolic functions, the vibrational contribution to α_S is $\alpha_{S,vib} = (k_B/q)\sum_i(-\Delta\omega_i/\omega_i)$. To calculate the transport Seebeck component $\alpha_{S,trans}$ related with the phonon-assisted hopping, additionally, we start from $\alpha_{S,trans,ep} = E_T/qT$, where subscript ep means polaron and E_T is the net vibrational energy that accom-

panies a phonon-assisted hopping, i.e.,[5,6,11,32]

$$E_T = \frac{k_B T^2}{2}[\frac{\partial\ln(\dot\gamma_{1,2}/\dot\gamma_{2,1})}{\partial T_1} - \frac{\partial\ln(\dot\gamma_{1,2}/\dot\gamma_{2,1})}{\partial T_2}]_{T_1=T_2=T}.$$
$$(8)$$

Here $\gamma_{1,2}$ (and $\gamma_{2,1}$) are the hopping rates between site 1 to site 2 at temperatures T_1 and T_2. Using the binding energy relation with the local stiffness[5,6,11,30], we have

$$E_T = E_a \sum_i(\frac{-\Delta\omega_i}{\omega_i})\frac{\hbar\omega_i/2k_B T}{\sinh(\hbar\omega_i/2k_B T)}. \qquad (9)$$

In this study, we approximate that $\alpha_{S,vib}$ and $\alpha_{S,trans}$ are the dominant contribution, since $\alpha_{S,mix}$ and $\alpha_{S,spin}$ are estimated to be negligible. These are justified due to heavy carrier density and non-ferromagnetic property for $B_{13}C_2$.

III. RESULTS AND DISCUSSION

A. Lattice dynamics and polaron formation

To understand the vibrational behavior of $B_{13}C_2$, we begin with their lattice dynamics and electronic structures using various DFT methods. Figure 2 shows total and projected phonon dispersion curves using small displacement method in the harmonic approximation. As we expected, $B_{13}C_2$, a hard solid material, has high phonon energy (up to 200 meV) showing its rigid bonds. As shown in Fig. 2(c), most intra- and inter-icosahedral bonds occupy acoustic and moderate optical parts, while the CBC chain bonds cover two local vibration modes [highest acoustic (~ 40) and optical (~ 190 meV)]. Despite the two-body (C-B_{chain}) bond in this chain having the shortest length (i.e. most rigid one) in $B_{13}C_2$, its three-body angle is the most flexible (due to limited neighbor atoms). Such Janus-faced CBC chain bond is unique in crystalline solids, and we suggest that this provides evidence of its abnormal transport properties.
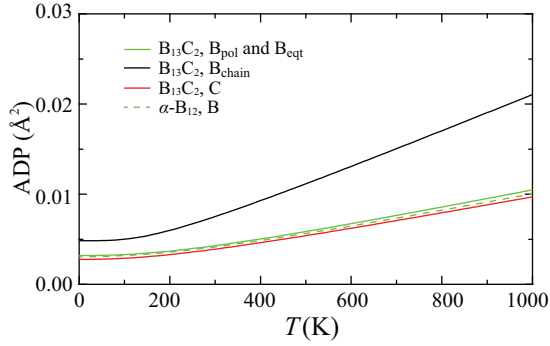
FIG. 3: (Color online) Variations of ADP with temperature for individual elements in $B_{13}C_2$ and α-B_{12}.
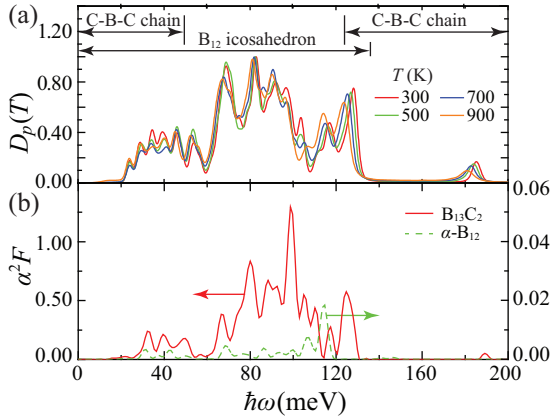

FIG. 4: (Color online) (a) Variation of total phonon density-of-states with temperature and (b) the Eliashberg function spectrum for $B_{13}C_2$.

Figure 3 shows the atomic displacement parameter (ADP) for each designated element in $B_{13}C_2$ and α-B_{12}. Due to the strong and stable covalent bonds[33], for the overall icosahedral atoms, there is no distinct ADP difference between the two structures. However, the ADP of chain B (B_{chain}) is twice that of icosahedral B (B_{pol} and B_{eqt} in $B_{13}C_2$ and α-B_{12}). This large ADP of B_{chain} atoms is one of distinct lattice behaviors of $B_{13}C_2$ and we expect scattering of the heat-conducting phonon wave as in rattlers[34–36]. Such phonon dispersion and atomic displacement features in $B_{13}C_2$ lattice are shown in Fig. 4(a). These show the phonon occupancy and roles contributed by each structural compartment of $B_{13}C_2$. Note that optical phonons of the icosahedral bonds and CBC chains result in the phonon softening and local vibrational frequency, respectively. In the optical frequency domain, the D_p is red-shifted as temperature increases. This phonon softening is critical in explaining the temperature independence of α_S. The B_{chain} atoms mostly lead to the local phonon mode of ~ 40 meV and weak force constant, one of reasons for low κ_L of $B_{13}C_2$. This is consistent with the local phonon dispersion and large ADP of B_{chain} atoms. Next, we show that phonon soft-ening is caused by the high-temperature Jahn-Teller distortion and polaron formation.

The e-p interaction is critical in explaining the unusual properties of $B_{13}C_2$[12,14,37,38]. The $\alpha^2 F$ characterizes the strength and spectrum of the e-p coupling in a system and is shown in Fig. 4(b) for $B_{13}C_2$ and α-B_{12}. Because $B_{13}C_2$ has high carrier density, significant e-p interactions are predicted, dominant in the icosahedral optical region, while α-B_{12} has negligible couplings. So, e-p couplings are highly related with the lattice dynamics of icosahedral structure and the trapped charge. Although the frozen structure of $B_{13}C_2$ (at 0 K) is an orthorhombic $R3m$ and high symmetry icosahedral complexes, we expect large geometrical distortion enhancing e-p interactions with increase in temperature, i.e., the Jahn-Teller distortion effect. The distortion and localized charge distribution of $B_{13}C_2$ result in polaron formation at high temperatures, and this causes bond softening. Figure 5(a) shows the low-symmetry lattice structure and the altered effective charge of each atom, and contrasting them with the frozen (ideal) structure. At $T = 0$ K, the B_{12} icosahedron loses its electrons, while the intra-icosahedral chain (CBC) is negatively charged. The effective charges of B_{eqt} and B_{pol} are +0.92 and -0.01e_c, and these are highly consistent in the overall structure. However, these conditions are not sufficient for polaron formation at low temperatures. Compared to that, the Jahn-Teller distortion activated by temperature makes for unique modifications in the charge distribution, as shown in Figs. 5(b) and (c). Also, the polaron formation accelerates the lattice distortion (bond softening) and traps the local charge within the distorted structure. The charge density (n_e) plot shown in Fig. 5(b) clearly shows the existence of polaron with the localized charges and lattice distortion. Comparing with high-symmetry position of ions (translucent color) shown in Fig. 5(c), highly-charged atoms (e.g., B_{eqt} with +2.4e_c) attract/repel adjacent ions depending on their polarity and accelerate the lattice distortions after producing the polarons. These are generally self-trapped, and cannot contribute to various transport properties at low temperatures, but several hopping mechanisms activated by temperature[5,6,30] are suggested. Next we show such phonon softening and polaron generation assisted by e-p interactions can affect the abnormal behaviors of α_S and κ_L in $B_{13}C_2$.

B. Prediction of Seebeck coefficient

We calculate the value of α_S for $B_{13}C_2$ using the DFT-based methods, and Fig. 6(b) results show that α_S becomes nearly independent of temperature above 600 K. Temperature-independent α_S is commonly observed in solids when high-temperature charge conduction is dominated by the hopping of constant-density small polarons[5,9].

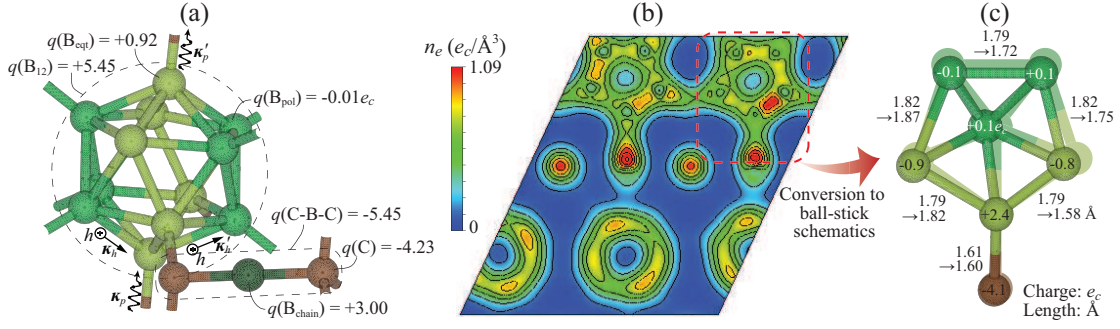Here, available experimental results[5] are confirmed with the direct method and entropy analyses using

FIG. 5: (Color online) The Jahn-Teller distortion and polaron formation of $B_{13}C_2$. (a) A presentation of carrier transport and averaged effective charge distribution at $T = 0$ K. (b) Contours of constant charge density, and (c) distorted icosahedron (area surrounded by a dashed line), at $T = 900$ K (for comparison, changes of bond length and ion positions between 0 and 900 K, and effective charges at $T = 900$ K are also shown).
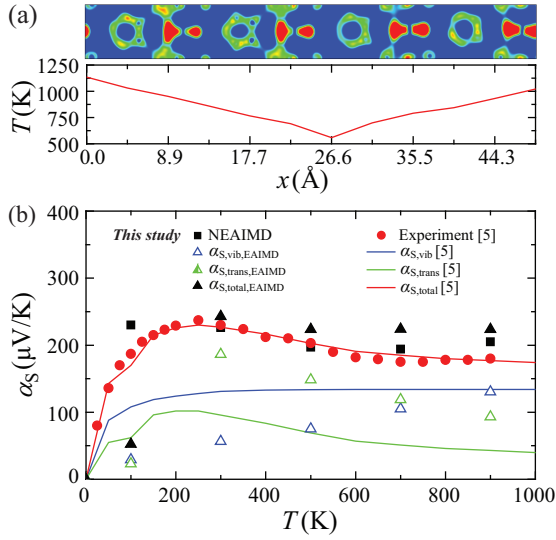

FIG. 6: (Color online) (a) Distributions of charge and temperature along the simulation cell. (b) Variations of $B_{13}C_2$ Seebeck coefficient and its components as a function of temperature. The NEAIMD, EAIMD and available experimental and model results are shown.

DFT. Using non-equilibrium *ab-initio* molecular dynamics (NEAIMD), we calculate α_S with this direct method, i.e., the charge difference under the applied temperature difference, $\alpha_S = -\Delta\varphi_e/\Delta T$[31]. Here, the potential difference ($\Delta\varphi_e$) is computed as the ratio of charge difference (Δq) and the electric permittivity over the prescribed temperature difference (ΔT) over a distance L, i.e.,

$$\Delta\varphi_e = \int_0^L \frac{n_e}{\epsilon_e\epsilon_\circ}\mathrm{d}x = \frac{\Delta q L}{\epsilon_e\epsilon_\circ A}, \qquad (10)$$

where ϵ_e and $\epsilon_\circ$ are the relative and free-space permittivities, and A is the cross-section area of the simulation cell. For the relative permittivity of $B_{13}C_2$, the experimental results[39,40] are used. We note that the low-temperature discontinuities in ϵ_e of $B_{13}C_2$ may be ignored because of the polarization and phase change of $B_{13}C_2$. The sim-

ulations details are given in the method section. Figure 6(a) shows the predicted charge distribution along the temperature gradient in the simulation cell. This snapshot shows the trapped charge and polaron generation in high-temperature icosahedra. The α_S obtained from Eq. (10) is plotted in Fig. 6(b), showing an initial sharp increase with temperature and temperature independence at high temperatures. These NEAIMD predictions agree well with the available experimental results[5].

To explain this unusual $\alpha_S(T)$ behavior, two different contributions to α_S are also shown in Fig. 6(b). Using the temperature-dependent D_p shown in Fig. 4(a) and Eq. (7), the high-temperature vibrational contributions to α_S are predicted. Charge carriers and their interactions cause a net energy transfer and in $B_{13}C_2$, the locally-induced polarons change the net energy transfer by employing deformation energy and hopping activation energy (E_a, ~ 0.17 eV)[5,7,9]. The transport contributions to α_S are calculated with $\alpha_{S,trans,ep} = E_T/qT$ and Eq. (9). As shown in Fig. 6(b), the component $\alpha_{S,vib}$ increases as the temperature increases, while $\alpha_{S,trans,ep}$ rises from zero, and reaches a peak at about 1/3 of the Debye temperature (T_D, ~ 750 K), and then falls to a small value. Thus, we verify that the phonon softening contributes to α_S in $B_{13}C_2$. The sum of these two contributions is in agreement with the temperature dependence of the α_S of $B_{13}C_2$ obtained from our NEAIMD and in experiments[5]. In the low-temperature regime, we note limitations in the extrapolated structural parameters and the AIMD formalism (e.g., constant-volume calculation). Also we note that the EAIMD results [$D_p(T)$, $\alpha_{S,vib}$, and $\alpha_{S,trans}$] are more complete thus differ from the simple approximations used by Emin[5,9]. The only two softening modes he used are 10 and 60 meV, i.e., one acoustic and one optical (albeit the lowest optical) mode. Based on our DFT predictions (Figs. 2 and 4), more relevant modes can be selected. Our results show that such low energy (acoustic) mode are not affected by the phonon softening, so approximate models should include the higher energy phonons.

C. Prediction of lattice conductivity

The lattice conductivity results of $B_{13}C_2$ are also obtained from the NEAIMD formulism as the the ratio of an applied heat flux to the resulting temperature gradient, i.e.,[24,25]

$$\kappa_L = -(\overline{Q(t)}/A)(\overline{dT/dz})^{-1}, \qquad (11)$$

where the overbar indicates time average and $Q(t)$ is the heat flow rate. Simulation details are given in the method section. In order to consider the size limitation of NEAIMD, we check the size effect with three different simulation cells (180, 270, and 360 atoms for $B_{13}C_2$).
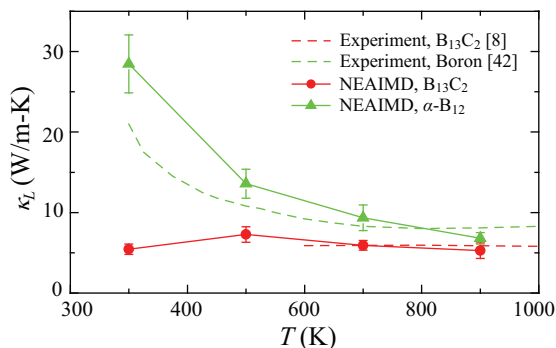

FIG. 7: (Color online) Variations of $B_{13}C_2$ and α-B_{12} lattice conductivity as a function of temperature. The NEAIMD and available experimental results are shown.

The κ_L of the infinite structure is determined from the linear extrapolation of their reciprocal relation (κ_L^{-1} versus L^{-1})[24]. The final κ_L results of $B_{13}C_2$ shown in Fig. 7 has a plateau behavior in overall temperature range. In order to emphasize this unusual temperature-independent κ_L behavior of $B_{13}C_2$, it is contrasted with the results for α-B_{12}, i.e., the Slack behavior ($\sim T^{-1}$)[31,41]. As discussed in the lattice dynamics and charge analyses, we find two distinct features, (i) significant e-p coupling, and (ii) large ADP of the chain bond, affecting κ_L. Based on the general temperature dependence of κ_L, various phonon scattering mechanisms dominate in their respective regimes[31]. At low temperatures ($T \ll T_D$), phonons are scattered by the grain-boundary, impurity, and electrons (most important here). The high temperatures ($T > 0.1T_D$) behavior is dominated by inter-phonon scattering and follows the Slack relation for long-range acoustic phonon transport. Although $B_{13}C_2$ and α-B_{12} have almost the same icosahedral structures, the uniqueness caused by the addition of carbon into α-B_{12}, makes for the high carrier density and the CBC chain (inter-icosahedral) bond. Significant e-p interactions in the icosahedra suppress the κ_L at low temperatures, while the large ADP of B_{chain} scatters the heat-conducting phonon waves and reduces κ_L at high temperatures. In contrast, the κ_L of α-B_{12}

is large and follows the Slack relation well. This is because there are no significant phonon scattering sources (e.g., e-p interactions and high ADP bonds). The predicted NEAIMD results are in good agreement with the experimental results[8,42].

IV. CONCLUSIONS

Boron carbides are common high-temperature materials having anomalous properties not yet well explained. Here we showed how their polarons and phonons are affected by the interaction between lattice dynamics and charge distributions. The bond softening and e-p coupling caused by the high-temperature Jahn-Teller distortion and polaron formation are observed in optical phonons of icosahedra. The unique atomic displacement of the CBC chain bonds shows significant interphonon scattering of the acoustic modes. These theoretical and computational treatments predict abnormal temperature independencies of the Seebeck coefficient and lattice conductivity, showing good agreement with experimental results. Understanding of such coupled phonon and polaron effects of $B_{13}C_2$ offers insights for new thermoelectric materials.

ACKNOWLEDGMENT

[*] Electronic address: `kaviany@umich.edu`

[1] V. Domnich, S. Reynaud, R. A. Haber, and M. Chhowalla, J. Am. Ceram. Soc. **94**, 3605 (2011).

[2] D. Emin, Phys. Today **40**, 55 (1987).

[3] T. L. Aselage and D. Emin, *Chemistry, Physics and Materials Science of Thermoelectric Materials: Beyond Bismuth Telluride* (Kluwer, Dordrecht, 2003).

[4] U. Kuhlmann, H. Werheit, and K. A. Schwetz, J. Alloys Compd. **189**, 249 (1992).

[5] T. L. Aselage, D. Emin, S. S. McCready, and R. V. Duncan, Phys. Rev. Lett. **81**, 2316 (1998).

[6] D. Emin, Phys. Rev. B **59**, 6205 (1999).

[7] M. Bouchacourt and F. Thevenot, J. Mater. Sci. **20**, 1237 (1985).

[8] C. Wood, D. Emin, and P. E. Gray, Phys. Rev. B **31**, 6811 (1985).

[9] T. L. Aselage, D. Emin, and S. S. McCready, Phys. Rev. B **64**, 054302 (2001).

[10] C. Wood and D. Emin, Phys. Rev. B **29**, 4582 (1984).

[11] D. Emin, *Polarons* (Cambridge, New York, 2013).

[12] H. Werheit, J. Phys.: Condens. Matter **19**, 186207 (2007).

[13] N. Vast, J. Sjakste, and E. Betranhandy, J. Phys.: Conf. Ser. **176**, 012002 (2002).

[14] M. Calandra, N. Vast, and F. Mauri, Phys. Rev. B **69**, 224505 (2004).

[15] D. M. Bylander and L. Kleinman, Phys. Rev. B **43**, 1487 (1991).

[16] G. Kresse and J. Furthmüller, Phys. Rev. B **54**, 11169 (1996).

[17] K. Parlinski, `PHONON` Software Package (Cracow, 2008).

[18] J. P. Perdew, K. Burke, and M. Ernzerhof, Phys. Rev. Lett. **77**, 3865 (1996).

[19] P. E. Blöchl, Phys. Rev. B **50**, 17953 (1994).

[20] G. Kresse and D. Joubert, Phys. Rev. B **59**, 1758 (1999).

[21] F. Thévenot, J. Euro. Ceram. Soc. **6**, 205 (1990).

[22] F. Muller-Plathe, J. Chem. Phys. **106**, 6082 (1997).

[23] P. Jund and R. Jullien, Phys. Rev. B **59**, 13707 (1999).

[24] S. Stackhouse, L. Stixrude, and B. B. Karki, Phys. Rev. Lett. **104**, 208501 (2010).

[25] D. Wang, L. Tang, M. Long, and Z. Shuai, J. Phys. Chem. C **115**, 5940 (2011).

[26] G. Henkelman, A. Amaldsson, and H. Jonsson, Comput. Mater. Sci. **36**, 254 (2006).

[27] P. Giannozzi, S. Baroni, N. Bonini, M. Calandra, R. Car, C. Cavazzoni, D. Ceresoli, G. L. Chiarotti, M. Cococcioni, I. Dabo, A. D. Corso, S. de Gironcoli, S. Fabris, G. Fratesi, R. Gebauer, U. Gerstmann, C. Gougoussis, A. Kokalj, M. Lazzeri, L. Martin-Samos, N. Marzari, F. Mauri, R. Mazzarello, S. Paolini, A. Pasquarello, L. Paulatto, C. Sbraccia, S. Scandolo, G. Sclauzero, A. P. Seitsonen, A. Smogunov, P. Umari, and R. M. Wentzcovitch, J. Phys.: Condens. Matter **21**, 395502 (2009).

[28] S. K. Bose, O. V. Dolgov, J. Kortus, O. Jepsen, and O. K. Anderson, Phys. Rev. B **67**, 214518 (2003).

[29] G. Profeta, M. Calandra, and F. Mauri, Nat. Phys. **8**, 131 (2012).

[30] D. Emin, Phys. Stat. Sol. B **205**, 385 (1998).

[31] M. Kaviany, *Heat Transfer Physics* (Cambridge, New York, 2008).

[32] D. Emin, Phys. Rev. Lett. **35**, 882 (1975).

[33] K. Shirai, H. Dekura, Y. Mori, Y. Fujii, H. Hyodo, and K. Kimura, J. Phys. Soc. Jpn. **80**, 084601 (2011).

[34] D. T. Morelli and G. P. Meisner, J. Appl. Phys. **77**, 3777 (1995).

[35] G. A. Slack, in *CRC Handbook of Thermoelectrics*, edited by D. M. Rowe (CRC, Boca Raton, FL, 1995).

[36] H. Chi, H. Kim, J. C. Thomas, X. Su, S. Stackhouse, M. Kaviany, A. Van der Ven, X. Tang, and C. Uher, Phys. Rev. B **86**, 195209 (2012).

[37] G. A. Samara, D. Emin, and C. Wood, Phys. Rev. B **32**, 2315 (1985).

[38] F. Giustino, J. R. Yates, I. Souza, M. L. Cohen, and S. G. Louie, Phys. Rev. Lett. **98**, 047005 (2007).

[39] H. Werheit, J. Phys.: Condens. Matter **18**, 10655 (2006).

[40] Collaboration: Authors and editors of the volumes III/17G-41D, O. Madelung, U. Rössler, and M. Schulz, (ed.) *SpringerMaterials - The Landolt-Börnstein Database* (Springer, 2013).

[41] G. A. Slack, Solid. State Phys. **34**, 1 (1979).

[42] G. A. Slack, D. W. Oliver, and F. H. Horn, Phys. Rev. B **4**, 1714 (1971).